Damage quantification in concrete under uniaxial compression using microcomputed tomography and digital volume correlation with consideration of heterogeneity

Shangyu Yang, Haizhou Liu, Lingtao Mao, Fangao Li, Bingjie Wei, Yang Ju, François Hild

▶ **To cite this version:**

Shangyu Yang, Haizhou Liu, Lingtao Mao, Fangao Li, Bingjie Wei, et al.. Damage quantification in concrete under uniaxial compression using microcomputed tomography and digital volume correlation with consideration of heterogeneity. Mechanics of Materials, 2024, 199, pp.105178. 10.1016/j.mechmat.2024.105178 . hal-04743622

HAL Id: hal-04743622
https://hal.science/hal-04743622v1

Submitted on 18 Oct 2024

HAL is a multi-disciplinary open access archive for the deposit and dissemination of scientific research documents, whether they are published or not. The documents may come from teaching and research institutions in France or abroad, or from public or private research centers.

L'archive ouverte pluridisciplinaire **HAL**, est destinée au dépôt et à la diffusion de documents scientifiques de niveau recherche, publiés ou non, émanant des établissements d'enseignement et de recherche français ou étrangers, des laboratoires publics ou privés.

Damage Quantification in Concrete under Uniaxial Compression Using Microcomputed Tomography and Digital Volume Correlation with Consideration of Heterogeneity

Shangyu Yang[1], Haizhou Liu[2], Lingtao Mao[1,3,*], Fangao Li[1], Bingjie Wei[1], Yang Ju[1,3] and François Hild[4]

[1] *School of Mechanics and Civil Engineering, China University of Mining & Technology, Beijing 100083, China*

[2] *Shenzhen Institute of Advanced Technology, Chinese Academy of Sciences, Shenzhen 518055, China*

[3] *State Key Laboratory for Fine Exploration and Intelligent Development of Coal Resources, China University of Mining & Technology, Beijing 100083, China*

[4] *Université Paris-Saclay, CentraleSupélec, ENS Paris-Saclay, CNRS LMPS - Laboratoire de Mécanique Paris-Saclay, 91190 Gif-sur-Yvette, France*

*Corresponding author**:** Lingtao Mao, E-mail: mlt@cumtb.edu.cn

Abstract Finite element-based digital volume correlation with mechanical regularization was utilized to measure the deformation fields in a concrete specimen under uniaxial compression based on in-situ (via microcomputed tomography) experiment. Heterogeneous and damage settings were introduced in the mechanical regularization. The mechanical response of the matrix and aggregates was investigated. The three-dimensional morphology of subvoxel microcrack openings was measured, the overall assessment and local depiction of concrete damage were quantified. Subvoxel microcrack openings greater than 0.26 vx were identified. The average maximum principal and average volumetric strains in the matrix were higher than those in the aggregates, and noticeable strain concentrations existed in the interfacial transition zone and pore edges. Microcracks initiated in the macroscopic elastic stage, whereas voxel-level crack openings were observed at 90% of the ultimate load. This study provides experimental support for further revealing the growth process of concrete damage.

Keywords concrete; digital volume correlation (DVC); in-situ CT scanning; subvoxel microcrack opening; damage development

1 Introduction

As a quasi-brittle multiphase composite material, the complexity of the phases within concrete induces discontinuities in its physical and mechanical properties (Giaccio, et al., 1998; Gupta, et al., 2022; Mazars, 1986). To provide reliable estimates for the integrity of building structures, investigating the relationship between the heterogeneity of multiphase concrete and its macroscopic nonlinear mechanical behavior is essential. Currently, many studies are being conducted on the mechanical response and damage growth of concrete using nondestructive techniques. Acoustic emission (AE) is utilized to assess internal damage in concrete and locate cracked regions. By analyzing the AE characteristic parameters, the safety performance detection and damage evaluation of concrete structures is obtained (Burud, et al., 2021; He, et al., 2023; Qin, et al., 2022; Zhang, et al., 2022). Based on digital image correlation (DIC), the deformation fields on concrete surfaces are measured, and their heterogeneity and crack propagation laws have been analyzed (Golewski, 2021; Lian, et al., 2022; Zhou, et al., 2021). However, AE cannot achieve accurate location of damaged regions inside concrete and cannot specifically describe the microcrack propagation process. DIC does not give access to internal deformation fields, which limits the scope for describing damage growth in concrete.

In recent years, the popularization and application of X-ray computed tomography (XCT) in the field of civil engineering materials have significantly promoted the research on damage mechanism in concrete (du Plessis, et al., 2019). XCT gives access to the 3D morphology and spatial distribution of various concrete phases at the microscopic level (Chung, et al., 2021; Jivkov, et al., 2013; Sun, et al., 2022; Wong, et al., 2005). The 3D morphology of cracks obtained using image processing techniques reflects the degree of damage (Hong, et al., 2022; Oesch, et al., 2020). Combined with in-situ testing devices, using volumetric images under different loading conditions, and statistically analyzing changes in image grayscale information based on stereological methods, internal damaged regions are identified (Ding, et al., 2022; Hong, et al., 2019; Tian, et al., 2019). However, limited by the resolution of CT, the initiation and propagation of cracks above the voxel scale have been the main topics for damage analyses, and there has been little quantitative research devoted to the growth process of subvoxel microcrack openings. As a quasi-brittle material, macrocracking of concrete often foreshadows the rapid loss of its load-bearing capacity (Ouyang, et al., 2022), and the cracking mechanisms identified at the voxel scale only indicate that damage

accumulation inside a sample has triggered a cross-scale transformation, which is different from the initial stage of damage development.

The combination of digital volume correlation (DVC) and XCT has enabled for full-field measurements and visualization of internal deformations (Germaneau, et al., 2007; Jiroušek, et al., 2011; Liu, et al., 2023; Mao, et al., 2021; Mao, et al., 2019), thereby providing a richer and more accurate measurement method for quantifying the internal deformation characteristics at the microscopic level and capturing local damage events. Using this method, scholars have conducted research on the deformation features of various cement-based (Hong, et al., 2022; Lorenzoni, et al., 2022; Zhang, et al., 2021) and concrete (Li, et al., 2023; Stamati, et al., 2021; Zhang, et al., 2023) materials under different loading conditions and have effectively measured kinematic fields. However, the DVC subset size is often large, resulting in low spatial resolutions and challenges in detecting microscale damage at the initial stages of loading. Research has been conducted on subvoxel opening detection based on local (Chateau, et al., 2018) and global (Tsitova, et al., 2022) DVC, but have not yet been performed for damage quantification and characterization based on microcrack quantification throughout the loading process. In addition, to reduce the adverse effects of scanning noise, insufficient contrast and other factors, mechanical regularization (Tsitova, et al., 2022), curvature regularization (van Dijk, et al., 2019), and other additional constraints have been introduced to enhance the robustness of DVC algorithms.

Based on in situ uniaxial compression experiments on concrete samples, this study employs global DVC with mechanical regularization to measure 3D deformation fields inside concrete throughout the loading process and quantitatively analyze the mechanical response of the concrete phases. The outline of the paper is as follows. In Section 2, the focus is mainly on the concrete sample preparation and in-situ uniaxial compression. Section 3 mainly introduces the mechanically regularized DVC analysis method. Section 4 conducts the measurement uncertainty analysis of DVC, and discusses its applicability in concrete examples. In Section 5, mechanically regularized DVC parameters are further analyzed and discussed. The internal deformation field of concrete is calculated to analyze the differences in mechanical response of different phases, and the 3D expansion morphology of subvoxel microcrack openings is measured. The influence of regions with poor mechanical properties on the failure of concrete is investigated. The 3D expansion morphology of subvoxel microcrack openings are measured, and the overall assessment and local

characterization of the internal damage process are quantified using stereological methods. The influence of regions with poor mechanical properties on the failure of concrete is investigated.

2 Material and Experiment

2.1 Sample Preparation and Determination of Mechanical Parameters

Ordinary Portland cement PO 32.5 was used and natural limestone with a gradation between 4 and 20 mm was selected as the coarse aggregates. The fine aggregates were medium-coarse sand with a mud content of less than 5 vol%. The aggregate size distribution is shown in Fig. 1. The above materials were mixed according to the proportion of cement : fine aggregate : coarse aggregate : water = 1 : 3 : 6 : 1. Hereinafter, 'aggregate' refers to the coarse aggregates, and 'matrix' corresponds to the mixture of cement, fine aggregates, and water. The mixture was poured into a 100 mm × 100 mm × 100 mm mold. After curing for 28 days, cube samples were processed into cylindrical specimens with a size of 25 mm in radius and 50 mm in height for uniaxial compression. An average peak stress of 22.4 MPa was measured for 3 samples using a CSS-44100 universal testing machine.

The constituent parameters are shown in Table 1. The densities of the aggregates and matrix were measured using the density test method. Nanoindentation tests were carried out to measure the reduced Young's modulus of mortar and aggregates. The Poisson's ratios correspond to literature data (Brandt, 2005; Claisse, 2015; Gercek, 2007; Ji, et al., 2018).

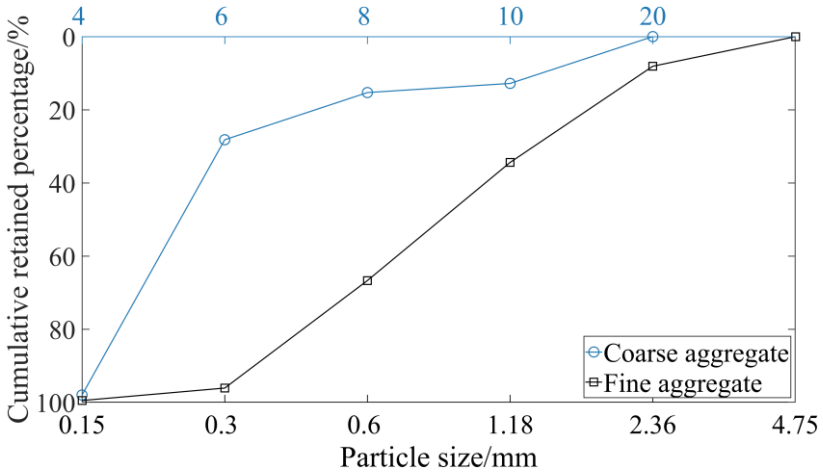

Fig. 1 Aggregate size distribution curve.

Table 1 Mechanical parameters of aggregates and matrix.

Material	Density (kg/m^3)	Young's modulus (GPa)	Poisson's ratio
Aggregate	2,660	49.4, 52.1, 54.1, 56.1, 58.8 (average: 54.1)	0.21
Matrix	2,100	10.5, 11.7, 12.7, 13.7, 14.9 (average: 12.7)	0.25

2.2 In-situ Uniaxial Compression

An in situ uniaxial compression experiment was conducted using a home-designed uniaxial loading device and a micro-CT system (Mao, et al., 2017). The scanning parameters are listed in Table 2.

Table 2 Micro-CT scanning parameters.

Item	Parameters
Detector	PerkinElmer XRD 0822AP 14
Definition	1024 × 1024 pixels
X-ray source	YXLON 225 kV
Scanning voltage/current	120 kV/0.2 mA
Scanning time	25 min
Resolution	45μm × 45μm × 45 μm
Number of projections	720
Rotation step	0.5°
Filter (reconstruction)	None
Gray-level amplitude	16 bits

The CT system and uniaxial loading device are shown in Fig. 2.

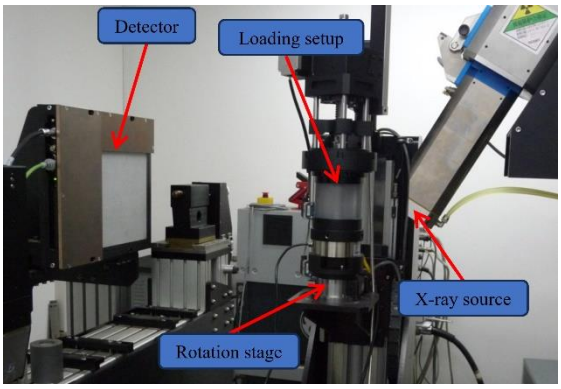

Fig. 2. CT system and uniaxial loading device.

Scanning was performed at 8 stress levels, namely, 0, 4.5, 9.0, 13.5, 16.0, 19.5, 21.6 MPa and after failure. During each scan, the loading was held constant. Due to 25 min duration of each scan (see Table 2), small stress relaxations occurred, which led to the some small oscillations in the stress–strain curve (Fig. 3(a)). Two scans were performed at 0 MPa to quantify measurement uncertainties. Volumes of interest with sizes 700 vx × 700 vx × 900 vx were cropped from the reconstructed images. The 3D renderings are displayed in Fig. 3(b, c). Fig. 3(c) shows that there is a tilted main crack and several secondary cracks virtually parallel to the *z*-axis, thereby indicating that tension-shear hybrid failure occurred in the specimen. The stroke speed was 0.18 mm / min.

In addition, two sections located at $x = 12.5$ mm and $y = 12.5$ mm (orthogonal to each other) are also shown (Fig. 3(d,f)). It is observed that the cracks propagated along aggregate-cement interfaces, which were bridged by cracks in the matrix to form the macrocrack. Among them, the green dashed regions are used for the analysis of kinematic fields (Section 5.1), and the white dashed regions are used in Section 5.2; the corresponding damaged sections are displayed together (Fig. 3(e,g)).

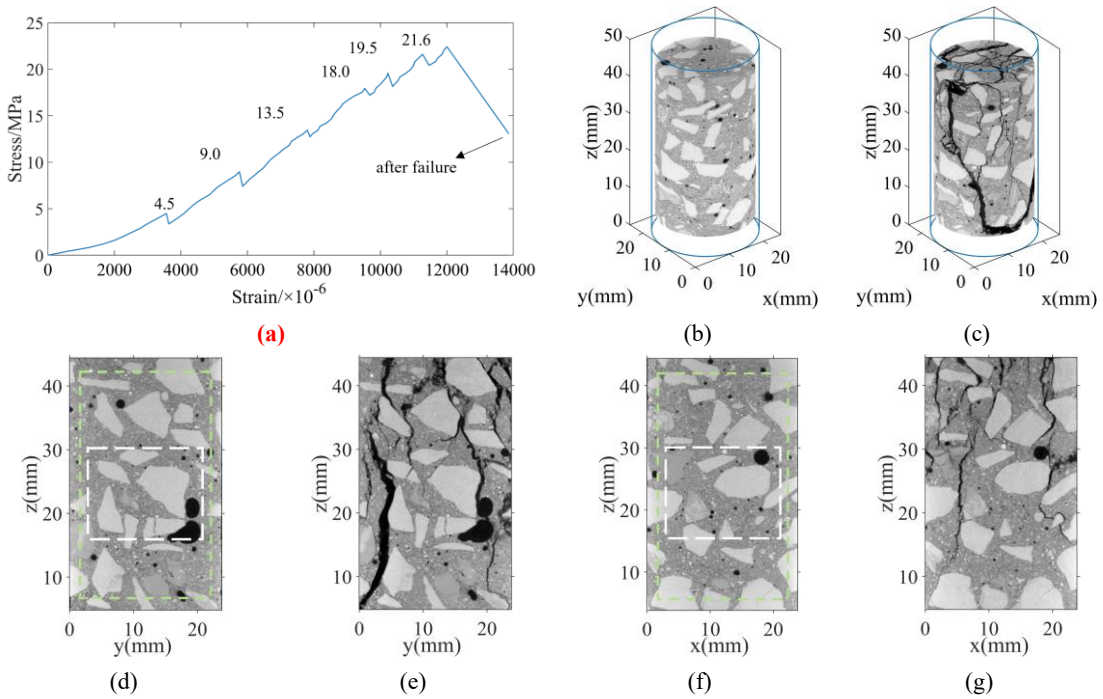

Fig. 3. (a) Stress–strain curve of in situ uniaxial compression. 3D renderings of the in situ tested sample at 0 MPa (b) and after failure (c). Section located at $x = 12.5$ mm at 0 MPa (d) and after failure (e). Section located at $y = 12.5$ mm at 0 MPa (f) and after failure (g).

3 Analysis Methods

3.1 Mechanically Regularized DVC

Reducing measurement uncertainty while increasing the spatial resolution is one of the key problems in DVC. In conventional DVC, large interrogation subsets or coarse meshes allow for a low uncertainly in the measured displacements at the expense of a poor spatial resolution. Conversely, small interrogation subsets or fine meshes induce a better spatial resolution, but due to the fewer voxels considered for each measured displacement, at the expenses of higher displacement uncertainties (Leclerc, et al., 2011). A tradeoff between spatial resolution and displacement uncertainly has to be found. In this study, regularization based on mechanical equilibrium was introduced in global DVC to lower this limitation. Further, in global DVC, finite element meshes can be made consistent with the different phases of concrete. It is then possible to assign different elastic properties in the mechanical regularization method, and thus take into account the heterogeneous nature of the concrete. Such approach is not (yet) possible in commercial DVC softwares.

Additionally, based on mechanically regularized DVC, the microcrack opening displacement can be more accurately quantified by incorporating damage whenever needed (Liu, et al., 2023). The heterogeneity of strain fields is better captured by considering different elastic moduli for each phase (Tsitova, et al., 2022). As shown hereafter, this approach effectively reflects and quantifies damage in heterogeneous materials such as concrete.

3.1.1 Basic Principle

The reference and deformed volumes are defined as $f(\mathbf{x})$ and $g(\mathbf{x})$, respectively, and the corresponding displacement field is $\mathbf{u}(\mathbf{x})$. Based on the gray level conservation principle

$$f(\mathbf{x}) = g(\mathbf{x} + \mathbf{u}(\mathbf{x})) \tag{1}$$

According to the finite element theory (Zienkiewicz, et al., 2005), the displacement field $\mathbf{u}(\mathbf{x})$ is expressed as

$$\mathbf{u}(\mathbf{x}) = \sum_i N_i(\mathbf{x}) u_i \tag{2}$$

where N_i is the i-th shape function, and u_i the corresponding nodal displacement. The gray-level residual (GLR) field φ_c and dimensionless correlation residual η are defined as

$$\varphi_c = \left| f(\mathbf{x}) - g\left(\mathbf{x}+\mathbf{u}(\mathbf{x})\right)\right| \tag{3}$$

$$\eta = \frac{\sqrt{\frac{1}{|\Omega|}\sum_{\mathbf{x}}\left(f(\mathbf{x}) - g(\mathbf{x}+\mathbf{u}(\mathbf{x}))\right)^2}}{f_{\max} - f_{\min}} \tag{4}$$

where Ω stands for the Region of Interest (ROI).

The displacement field $\mathbf{u}(\mathbf{x})$ is obtained by minimizing the following cost-function

$$\min_{\{\mathbf{u}\}} \Phi_c^2 = \sum_{\Omega}\left[f(\mathbf{x}) - g\left(\mathbf{x}+\mathbf{u}(\mathbf{x})\right)\right]^2 \tag{5}$$

using a Gauss-Newton iterative scheme (Hild, et al., 2012)

$$[\mathbf{M}]\{\delta\mathbf{u}\} = \{\mathbf{b}\} \tag{6}$$

where $\{\delta\mathbf{u}\}$ is the column vector gathering all incremental nodal displacements, and

$$M_{ij} = \int_{\Omega}\left(\nabla f(\mathbf{x})\cdot \boldsymbol{N}_i(\mathbf{x})\right)\left(\nabla f(\mathbf{x})\cdot \boldsymbol{N}_j(\mathbf{x})\right)\mathrm{d}\mathbf{x} \tag{7}$$

$$b_i = \int_{\Omega}\left(\nabla f(\mathbf{x})\cdot \boldsymbol{N}_i(\mathbf{x})\right)\left(f(\mathbf{x}) - g\left(\mathbf{x}+\mathbf{u}(\mathbf{x})\right)\right)\mathrm{d}\mathbf{x} \tag{8}$$

When measuring displacement fields, in addition to considering the matching degree of the grayscale information between the reference and deformed images, it may also satisfy the corresponding mechanical equilibrium conditions. Mechanically admissible solutions are obtained by adding equilibrium conditions. In a finite element sense, the balance equations read

$$[\mathbf{K}]\{\tilde{\mathbf{u}}\} = \{\mathbf{f}\} \tag{9}$$

where $[\mathbf{K}]$ is the full stiffness matrix, $\{\tilde{\mathbf{u}}\}$ nodal displacement vector, and $\{\mathbf{f}\}$ the nodal force vector. A new cost-function Φ_m is defined as the mechanical residual assessing the equilibrium gap

$$\{\mathbf{f}_r\} = [\mathbf{K}]\{\mathbf{u}\} - \{\mathbf{f}\} \tag{10}$$

In the absence of body forces, the applied forces on all internal nodes are null. Therefore, the corresponding cost-function reads (Hild, et al., 2015)

$$\Phi_m^2 = \{\mathbf{u}\}^{\mathrm{T}}[\mathbf{K}]^{\mathrm{T}}[\mathbf{K}]\{\mathbf{u}\} \tag{11}$$

Therefore, the displacement field is obtained by minimizing the weighted sum of dimensionless cost-functions (5) and (11) (Leclerc, et al., 2012; Leclerc, et al., 2011)

$$\Phi_t^2 = \tilde{\Phi}_c^2 + \omega \tilde{\Phi}_m^2 \tag{12}$$

where $\tilde{\Phi}_c^2$ and $\tilde{\Phi}_m^2$ denote normalized gray residuals and mechanical residuals, respectively. They are obtained by considering a reference displacement field associated with a plane wave (of wave vector $\boldsymbol{k}$). The weight ω is defined as (Leclerc, et al., 2012)

$$\omega = \left(2|\boldsymbol{k}|\pi \ell_{reg}\right)^4 \tag{13}$$

where ℓ_{reg} is the so-called regularization length.

In the present algorithm, 8-noded cubic elements are utilized. Thus, the algorithm is called Reg-C8-DVC, which is implemented in MATLAB. Mechanical regularization is considered only for internal nodes

3.1.2 Stiffness Matrix

The stiffness matrix reflects the load response of the material. In the present case, the stiffness matrix is constructed as follows:

(1) Considering material heterogeneity in the stiffness matrix

In mechanically regularized DVC considering elastic heterogeneities, the regularization weight varies between phases since it depends on the Young's modulus. According to the phase in each element, the elastic properties are set accordingly. Therefore, elastic contrast C is accounted for (Tsitova, et al., 2022)

$$C = \frac{E_a}{E_m} = \left(\frac{\ell_{reg}{}^a}{\ell_{reg}{}^m}\right)^2 \tag{14}$$

where E_m and E_a are the Young's moduli of the matrix and aggregates, respectively. From such definition, it follows that the regularization weight is different in both considered phases.

(2) Damaging the stiffness matrix

The premise of using ℓ_{reg} is the assumption of elastic behavior when writing mechanical equilibrium. Therefore, for a damaged region where degradations initiated upon loading or were present initially (e.g., pores or initial cracks), a damage variable is added to weaken the elastic properties (Hild, et al., 2015). The elementary stiffness matrix $[\mathbf{K}_D^e]$ is expressed as

$$[\mathbf{K}_D^e] = [\mathbf{K}^e](1-D) \tag{15}$$

where $[\mathbf{K}^e]$ is the elementary stiffness matrix of an undamaged element, and $D \in$ [0, 1] the damage variable, which is uniform in each damaged element. If the element is fully damaged, D

should reach 1. In actual calculations, for damaged elements, D is made close to (but not equal to) 1 to ensure DVC convergence for small elements in which contrast is not high enough. The introduction of the damage variable D allows the mechanical regularization to be significantly weakened in non-elastic regions, while elastic regions remain under the control of mechanical regularization. The heterogeneous effect is schematically illustrated by connecting nodes with equivalent springs with different stiffness coefficients k_{ij}^{e}. The effect of damage is equivalent to connecting the nodes in the damaged region with weak springs whose stiffness tends to 0 as depicted in Fig. 4.

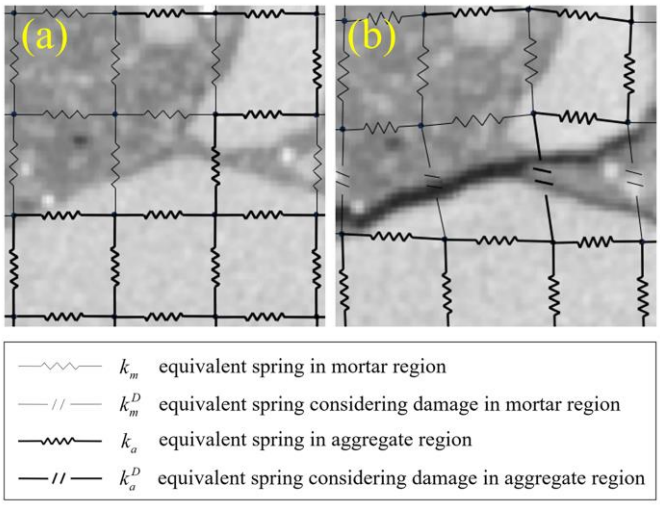

Fig. 4. Schematic illustration of the stiffness matrix with elastic contrast (a) and damage (b).

3.1.3 Crack Opening Displacement

The direct analysis of CT images allows cracks to be detected above the resolution scale when they are open. Newly generated subvoxel opening microcracks are characterized by the mean crack opening displacement (COD) in each damaged element (Liu, et al., 2023)

$$u_c = \varepsilon_1 l \tag{16}$$

where u_c is the elementary COD, ε_1 the maximum principal strain, and l the element size.

3.2 CT image segmentation

To run heterogeneous Reg-C8-DVC, a fine segmentation was performed using a U-net network (Ronneberger, et al., 2015), which distinguishes different phases without relying on traditional threshold-based segmentation methods. To enhance the training efficiency and reduce redundant information, a labeling strategy was adopted, every 50 CT slices from reference volume, one slice

was selected, during which the region of interest (ROI), including aggregates and pores, was manually labeled. To increase data diversity, data augmentation techniques such as rotation, mirroring, and contrast adjustment were applied. An 80% subset of the samples was chosen for training, with the remaining 20% utilized as the test set. The U-net model was then trained using these data and subsequently applied to all CT slices. The segmentation results are illustrated in Fig. 5. Among them, there are 1,393 pores, accounting for 1.93% of the sample volume, and the average equivalent diameter is 590 μm.

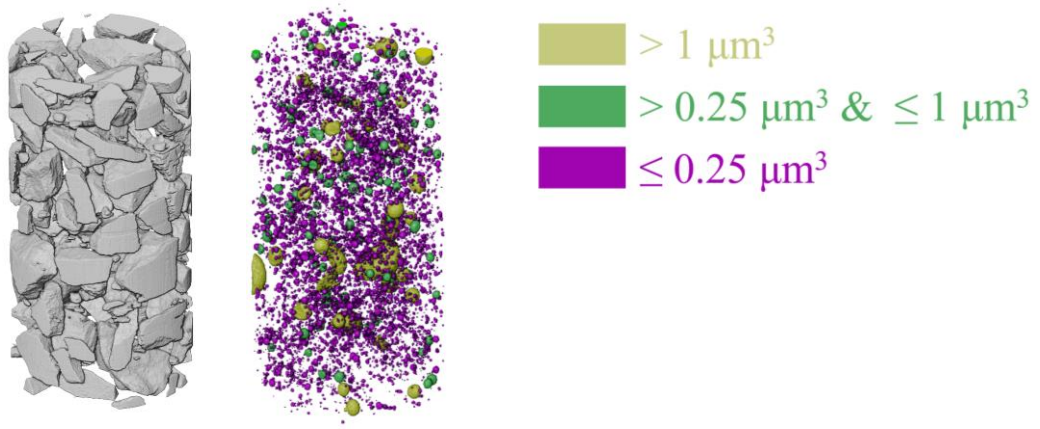

(a) (b)

Fig. 5 . Aggregate (a) and pore (b) segmentation.

4 DVC Analyses

4.1 Autocorrelation Examination

Reconstructed volumes are registered via DVC to measure deformation fields. Its feasibility needs to be checked before running Reg-C8-DVC analyses. Normalized autocorrelation curves with half-peak full width estimates (Minguet, et al., 2020) are used as a means of estimating the equivalent speckle size to characterize the richness of grayscale information in the ROI (Fig. 6). Fifteen regions with a size of 50 vx × 50 vx × 50 vx were randomly selected in the matrix, aggregates, and GLR (calculated using Reg-C8-DVC between two scans before loading, representing the baseline levels associated with acquisition noise and reconstruction artifacts), and their average equivalent speckle size was calculated.

Statistically, GLRs have a small average equivalent speckle size of less than 2 vx. The average equivalent speckle sizes of the aggregates and matrix were 3.3 and 6.6 vx, respectively. In summary,

the image grayscale information inside the concrete sample is sufficient to achieve scale separations between noise and contrast in both phases.

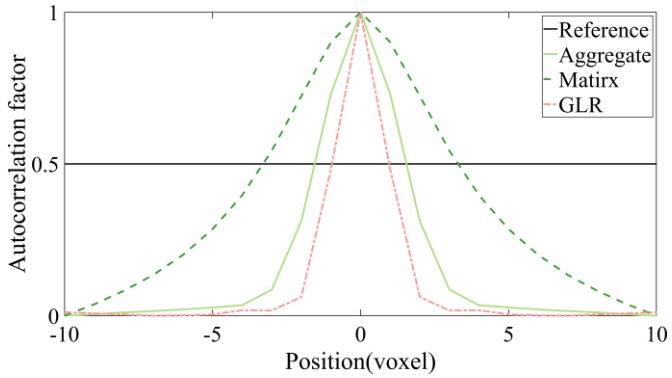

Fig. 6. Normalized autocorrelation function and equivalent speckle size associated with GLR and both phases.

4.2 Uncertainty Quantification

4.2.1 Parameter Setting

The two scans at 0 MPa were used to evaluate the measurement uncertainties associated with Reg-C8-DVC. A ROI of size 280 vx × 280 vx × 280 vx (i.e., 12.6 mm × 12.6 mm × 12.6 mm) in the middle of the concrete sample was cropped, as illustrated in Fig. 7(a). A uniform elastic contrast $C \equiv 1$ means homogeneous Reg-C8-DVC; otherwise, it is referred to as heterogeneous. Finite elements distinguished with different phases are shown in Fig. 7(b). The different parts represent the aggregates, matrix, and pore elements, respectively. The Reg-C8-DVC parameters are listed in Table 3. When considering heterogeneous Reg-C8-DVC, the regularization weight in different phases is affected by the Young's modulus (for the aggregates, it is equal to 54.1 GPa, and 12.7 GPa for the matrix). In the present case, the elastic contrast C between the aggregates and the matrix is equal to 4.26 (Equation (14)). Pores correspond to initial damage, and mechanical regularization also needs to be weakened. The damage variable D should be equal to 1 for fully damaged elements (Equation (15)). Considering the convergence of DVC calculations, such value cannot be set, and a value of 0.98 was selected, which is equivalent to 0.02 for C.

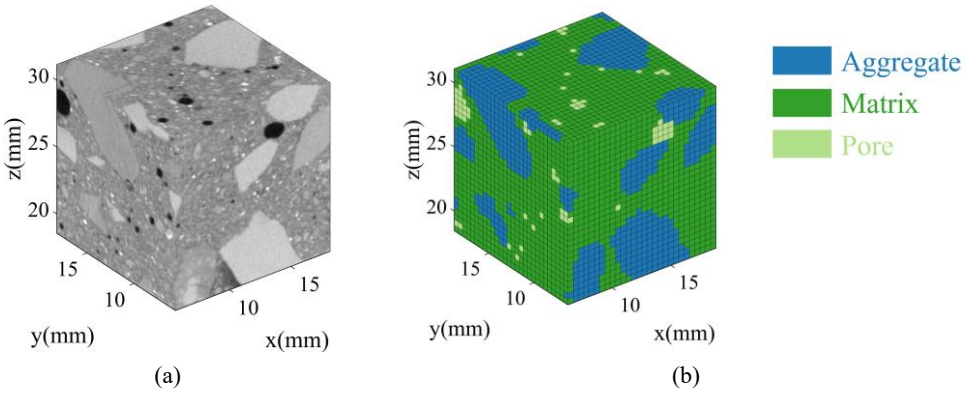

Fig. 7. Calculation region (a) and element labeling (b).

Table 3 Reg-C8-DVC parameters with homogeneous (first row) and heterogeneous elastic contrast.

Element division	Element type	Element size (vx)	Element number	Elastic contrast C
-	C3D8	11	21,952	1
Aggregate			7,322	4.26
Matrix			14,357	1
Pore			273	0.02

4.2.2 Residual Analysis

Fig. 8 depicts the changes of the dimensionless correlation and mechanical residuals with ℓ_{reg} when $C \equiv 1$ (Reg-C8-DVC was run using the volumes from the two scans acquired before loading). It is seen that as ℓ_{reg} decreases, the dimensionless correlation residual very slightly decreases from 8.1×10^{-3} to 7.7×10^{-3}. This effect is due to the fact that as the regularization weight is lowered, the total cost-function is less penalized and more freedom is given to the DVC analysis. Moreover, a decrease in ℓ_{reg} lowers the dimensionless weight ω, thereby reducing the constraint on mechanical equilibrium. Thus, the mechanical residuals significantly increase from 1.64×10^{-3} to 1.59×10^{4} (in arbitrary units).

The above results show that selecting a large regularization length ℓ_{reg} does not significantly degrade the dimensionless correlation residual. In the present case, the regularization length can be increased at will to act as a low-pass filter on the displacement field, which will filter out any non-mechanically admissible component (for instance, due to uncertainties associated with acquisition and CT reconstruction), which effectively improves Reg-C8-DVC.

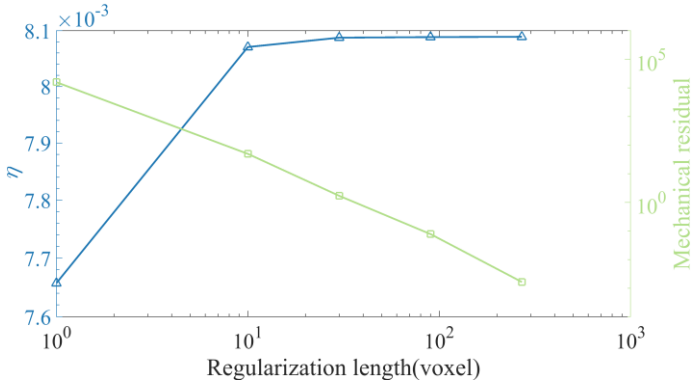

Fig. 8. Dimensionless correlation residual η and mechanical residual as functions of the regularization length ℓ_{reg} .

4.2.3 Displacement and Strain Uncertainties

Fig. 9 shows the displacement and strain uncertainties along the *x*-, *y*-, and *z*-axes of the aggregates (Fig. 9(a,c)) and matrix (Fig. 9(b,d)) as functions of ℓ_{reg} when $C \equiv 1$. As ℓ_{reg} increases, the higher mechanical admissibility, the more spurious fluctuations are filtered out. Therefore, when ℓ_{reg} is large, the uncertainties in the aggregate are lower than those in the matrix. When ℓ_{reg} = 10 vx, the standard displacement and strain uncertainties in the matrix are significantly smaller than those in the aggregates. This result is due to the fact that the regularization effect is relatively small, and the standard displacement uncertainty is inversely proportional to the image gradient, that is, the larger the image gradient, the smaller the standard measurement uncertainty (Leclerc, et al., 2012; Tsitova, et al., 2022). The root mean square of gray level gradient in the aggregate and matrix regions along the *x*-, *y*- and *z*-axes are calculated. In the aggregate region, it is equal to 138, 141 151 GL / vx and it is larger in the matrix, namely, 222, 221, 244 GL / vx.

The double logarithmic plots of Fig. 9 are also interpolated by power laws. For images corrupted by white Gaussian noise, the theoretical exponents of displacement and strain uncertainties are −1.5 and −2.5, respectively (Leclerc, et al., 2012). It is observed that the displacement (Fig. 9(a, b)) and strain (Fig. 9(c, d)) uncertainties of both aggregate and matrix regions approach the theoretical predictions.

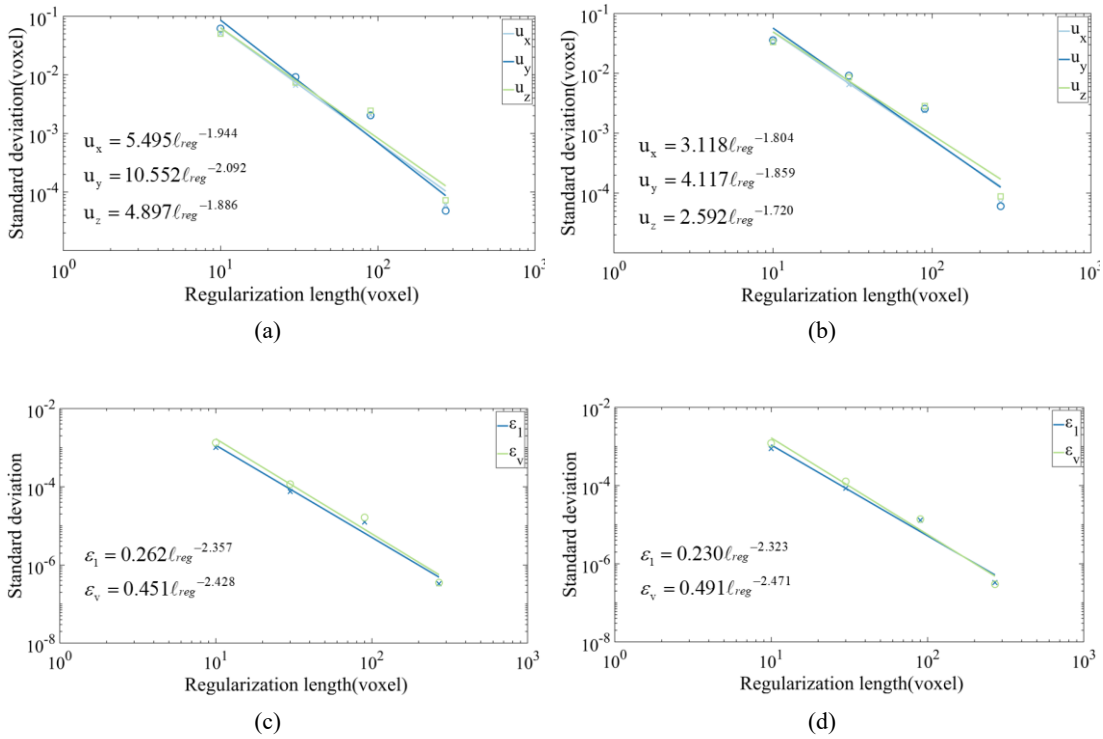

Fig. 9. Standard displacement (a, b) and strain (c, d) uncertainties versus regularization length ℓ_{reg} for the aggregates (a, c) and the matrix (b, d).

4.2.4 Effect of Mechanical Regularization

To assess the effect of mechanical regularization associated with Reg-C8-DVC, the dimensionless correlation residuals are plotted against the mechanical residuals at each loading stage using homogeneous and heterogeneous Reg-C8-DVC (Fig. 10). With increased loading, the change in the value of elastic contrast C influences more the Reg-C8-DVC results. For the same regularization length ℓ_{reg}, the mechanical residuals are higher when considering heterogeneity in Reg-C8-DVC. This effect occurs because the regularization weights in the different phases are different (i.e., the Young's modulus of the aggregates is 4.26 times that of the matrix; therefore, the regularization length in the aggregates is 2.1 times that in the matrix region with heterogeneous Reg-C8-DVC). Displacement gradients along the boundaries between different phases are also more pronounced.

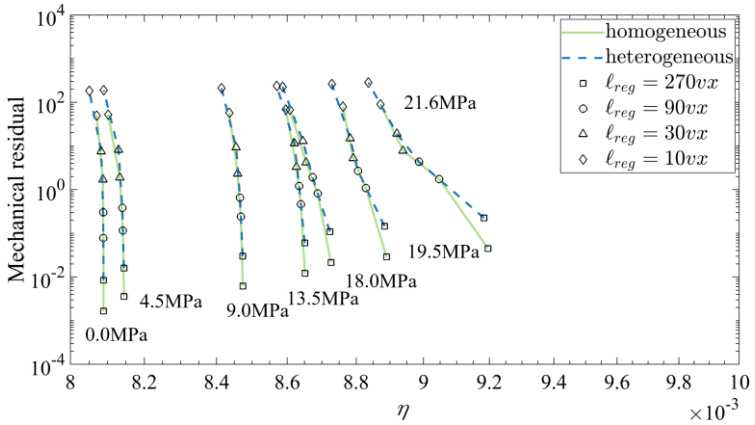

Fig. 10. Dimensionless correlation residual η vs. mechanical residual (in arbitrary units) using different Reg-C8-DVC approaches for each loading stage.

5 Analysis of Kinematic Fields

5.1 Overall Region of Interest

Reg-C8-DVC was run over the full height of the sample, 800 slices with a radius of 10.1 mm from 1.8 mm to 37.8 mm along the *z*-axis were kept, and the volume was 12.13 cm^3. First, the influences of Reg-C8-DVC parameters on the displacement fields were investigated. Then, the internal mechanical response of concrete was analyzed based on the deformation field. The mesh size was 21 vx, ℓ_{reg} was equal 180 vx, containing 16,520 elements and 18,860 nodes in total. For the kinematic analysis, the sections indicated in Fig. 3(d, f) (green dashed region) were used for illustration purposes.

5.1.1 Influence of Regularization Length

To select ℓ_{reg}, the dimensionless correlation and mechanical residuals are studied using heterogeneous Reg-C8-DVC at each loading stage (Fig. 11). It is observed that the lower the loading level, the more the curves tend to be parallel to the *y*-axis, thereby validating the hypothesis of heterogeneous elasticity. The dimensionless correlation residual degrades more as the applied load increases. For the mechanical residual, as internal damage develops within the material, it gradually deviates from the assumption of elasticity. The above factors lead to an increasing trend for both phases with an increase in loading under the same regularization length ℓ_{reg}. From Section 4.2.3, it was concluded that the larger ℓ_{reg}, the lower the measurement uncertainty. However, an excessively large ℓ_{reg} leads to excessive smoothing of displacement fields and cannot fully

capture the true kinematics.

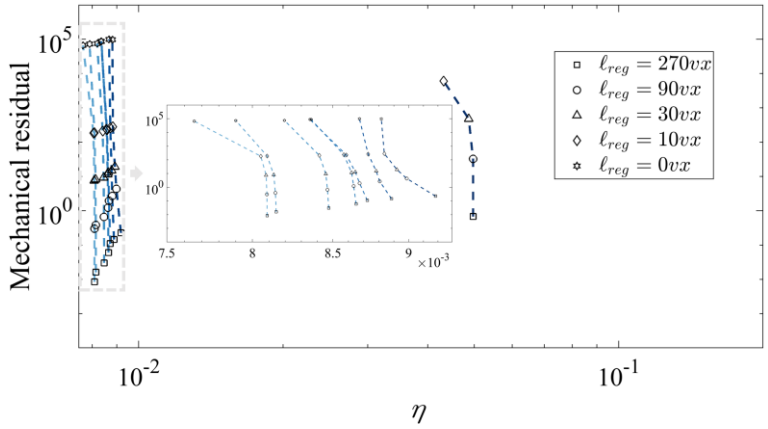

Fig. 11. Dimensionless correlation residual η vs. mechanical residual (in arbitrary units) using heterogeneous Reg-C8-DVC at each loading stage up to failure.

Considering the above results, a regularization length of nine times the element size was selected. Therefore, the standard displacement uncertainties in the aggregates and matrix are 2.2×10^{-3} vx and 2.6×10^{-3} vx, respectively. The maximum principal strain uncertainties are 1.3×10^{-5} and 1.3×10^{-5}, and the volumetric strain uncertainties are 1.6×10^{-5} and 1.4×10^{-5}, respectively.

5.1.2 Influence of Heterogeneous Weighting

To further elucidate the influence of applying heterogeneous weighting on the kinematic fields, Reg-C8-DVC was run on the volume image acquired at 21.6 MPa. Measured kinematic fields are shown in Fig. 12, in which the sections correspond to the green dashed regions in Fig. 3(d,f), respectively. It is seen from Fig. 12(b) that when heterogeneous Reg-C8-DVC is used, the displacement gradient in the dotted boxes changes more significantly than homogeneous Reg-C8-DVC (Fig. 12(a)). In the strain fields calculated by heterogeneous Reg-C8-DVC (Fig. 12(d)), the difference of mechanical response of the different phases is more clearly observed than that calculated by homogeneous Reg-C8-DVC (Fig. 12(c)). Statistics on the GLRs show that the values are 4.33×10^{-3} and 4.24×10^{-3} when using homogeneous and heterogeneous Reg-C8-DVC, respectively, thereby indicating that applying elastic contrast C improves the faithfulness of DVC analyses.

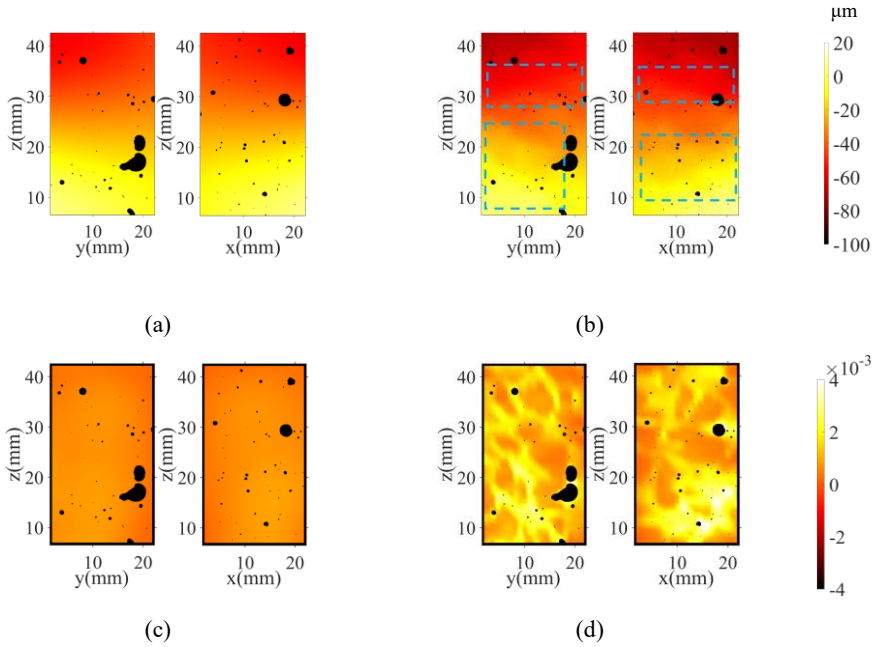

Fig. 12. Kinematic fields for homogeneous (a,c) and heterogeneous (b,d) regularization. Displacement fields along the *z*-axis (a,b). Maximum principal strain fields (c,d).

5.1.3 Influence of Damage Level

The damaged elements were identified using gray level hierarchical difference detection. The element-wise GLR obtained by Reg-C8-DVC of the two scans before loading was taken as the reference (GLR_A, Fig. 13(a)). The elementary GLR field obtained with Reg-C8-DVC for the volume after failure was considered (GLR_B, Fig. 13(b)) for comparison purposes. The criterion for selecting damaged element DE is such that GLR_{DE} satisfy

$$\Delta GLR = \left| GLR_B - GLR_A \right| \tag{17}$$

$$\Delta GLR_{DE} - \text{mean}(\Delta GLR) \geq 1.5 \times \text{std}(\Delta GLR) \tag{18}$$

The damaged elements extracted were then screened in combination with the spatial distribution of cracks after failure, the spatial distribution of damaged elements is shown in Fig. 13(c). To determine the influence of the damage level on Reg-C8-DVC, the damage variable was set as D = 0, 0.1, 0.5, 0.9, and 0.99, and Reg-C8-DVC was carried out on the volume acquired at 21.6 MPa to select an appropriate level.

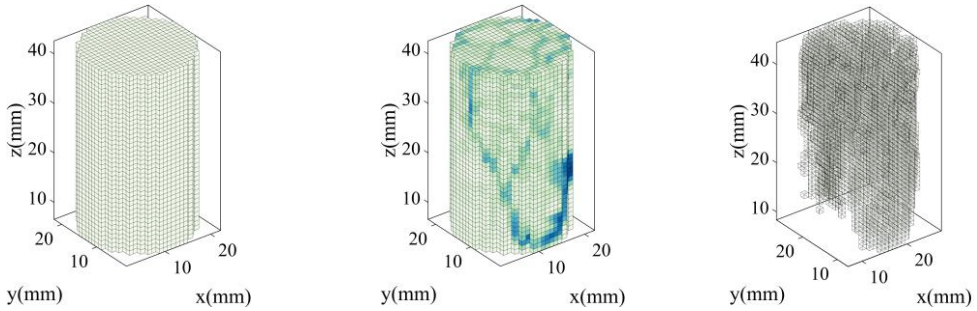

Fig. 13. Identification of damaged elements. (a) Reference GLR field. (b) Comparison GLR field. (c) Damaged elements.

Fig. 14 shows that as the damage level increases, the mean and root mean square GLR decrease, thereby indicating that the higher the damage level D, the more trustworthy Reg-C8-DVC. When $D = 0.99$, the dimensionless correlation residual is equal to 4.2×10^{-3}.

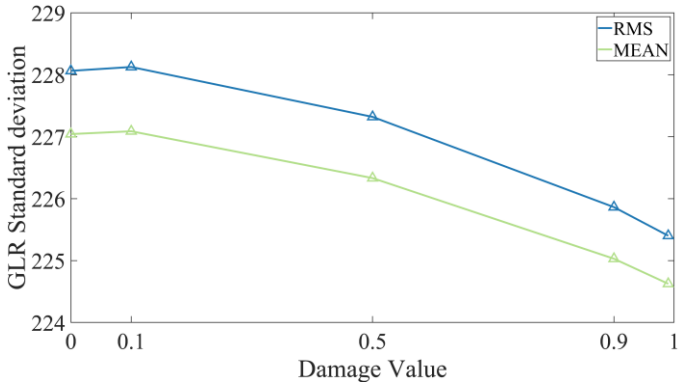

Fig. 14. Curves between damage factor value and GLR.

It is observed that as D increases, the displacement gradients in Fig. 15(a) and strain concentrations in Fig. 15(b) are more pronounced. Combined with the data of concrete sections after failure, the strain concentration regions correspond to the cracked regions. In all subsequent calculations, $D = 0.99$.

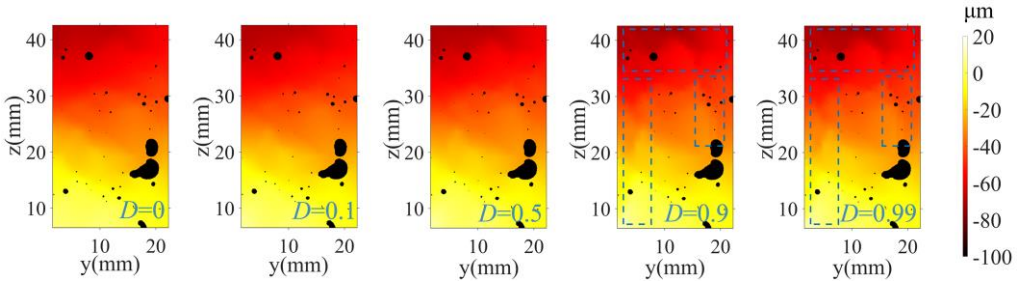

(a)

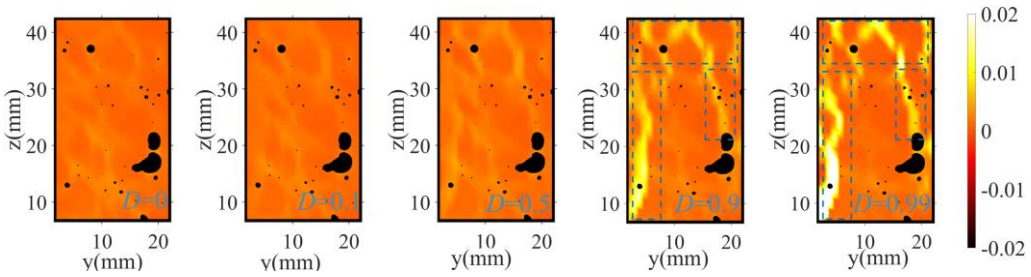

(b)

Fig. 15. Influence of damage values on kinematic fields. (a) Displacement fields along the *z*-axis. (b) Maximum principal strain fields.

It is seen from the introduction of the first three sections that a proper ℓ_{reg} fully captures the real kinematics while maintaining the assumptions of elasticity. The application of heterogeneous weighting C more accurately reflects the difference in mechanical response between the different phases, thus improving the accuracy and faithfulness of the DVC analyses. The addition of higher damage level D more accurately accounts for the fracture behavior of concrete during the stress process. It better capture the damage distribution inside the concrete sample.

5.1.4 Displacement Fields

The displacement changes in concrete during the full loading process in the green dashed regions (Fig. 3(d,f)) are shown in Fig. 16. As the applied load gradually increases, the displacement gradient amplitudes significantly increase in all directions. The sample is compressed along the *z*-axis and expands along the *x*- and *y*-axes. As the load increases, the displacement field concentrates in local regions of concrete (indicated by the dashed boxes).

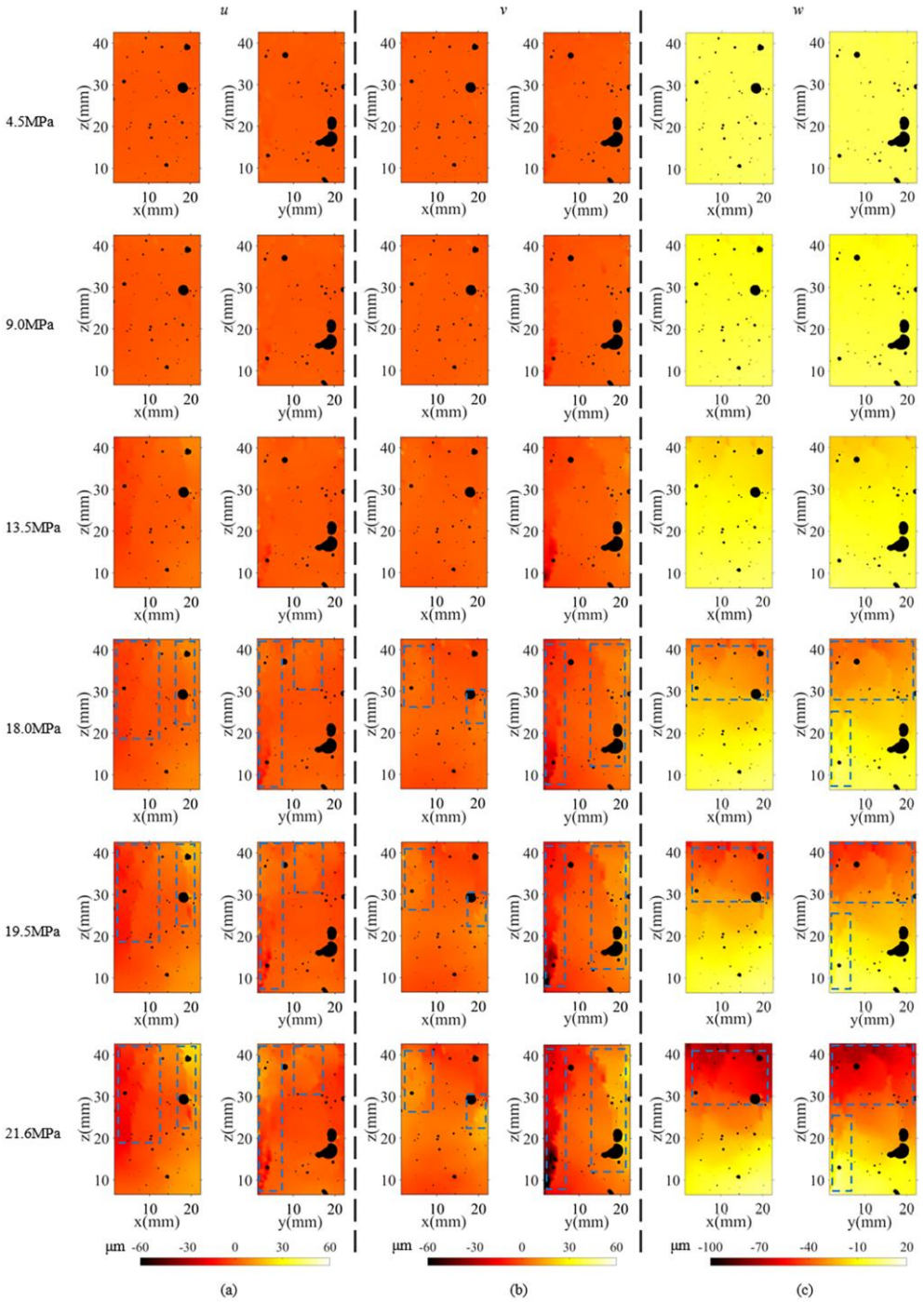

Fig. 16. Displacement field along the *x*-, *y*- and z- axes at 4.5, 9.0, 13.5, 18.0, 19.5, 21.6 MPa.
(a) *u* displacement; (b) *v* displacement; (c) *w* displacement fields.

5.1.5 Strain Fields

The macroscopic response of concrete results from coupled mechanical contributions of its internal phases. To determine the difference in mechanical responses of the internal phases (i.e., calculating the average maximum principal strain and volumetric strain for each loading stage), the

average strain changes in the aggregate and matrix elements were statistically analyzed separately.

Fig. 17(a) displays the average maximum principal strain in concrete, which increased with the applied load. The variation at the macroscopic level was similar to that of the matrix because its volume fraction was 61%. At 4.5 MPa, the average strains in the aggregate and matrix elements (which were equal 5.5×10^{-5} and 4.5×10^{-5}, respectively) were both greater than the measurement uncertainty. As the loading increases, the average maximum principal strains of both phases exhibited an increasing trend, and the difference in mechanical responses gradually became significant. At 21.6 MPa, the average maximum principal strains in the aggregates and matrix were equal to 9.8×10^{-4} and 3.7×10^{-3}, respectively.

From Fig. 17(b), it is observed that at 4.5 MPa, the average volumetric strain only reached -9×10^{-5}, which means that concrete was in an overall contraction state. At 9.0 MPa, the volumetric strain was equal to -10^{-5}, which was less than the measurement uncertainty, thus indicating that the strain had started to recover, that is, damage had occurred inside the sample. Therefore, 9.0 MPa is considered as the initiation point for damage development. At 13.5 MPa, the volumetric strain was equal to 5.8×10^{-4}, signifying that the sample was beginning to expand. At 21.6 MPa, the volumetric strain was 1.6×10^{-3}. From the changes in strains in the aggregates and matrix, it is concluded that at 4.5 MPa, the volumetric strain in the aggregates was very small (-2×10^{-6}), which was less than the measurement uncertainty, whereas the volumetric strain in the matrix was equal to -10^{-4}, which was a contraction state. At 9.0 MPa, the volumetric strains in the aggregates and matrix were 2.3×10^{-6} and -1.3×10^{-5}, both of which were less than the measurement uncertainty. In combination with the analysis at 4.5 MPa, it is observed that the volume of the matrix began to reverse at 9.0 MPa. At 13.5 MPa, the volumetric strains in the aggregates and matrix increased significantly and were both positive, indicating that their volume had expanded. However, at 18.0 MPa, the volumetric strains in the aggregate and matrix decreased to -1.2×10^{-4} and 1.5×10^{-4}, respectively, indicating that the internal strain structure changed at this level. Subsequently, the volumetric strain continued to increase with the applied load. At 21.6 MPa, the average volumetric strains in the aggregates and matrix were equal to 4.2×10^{-4} and 1.7×10^{-3}, respectively.

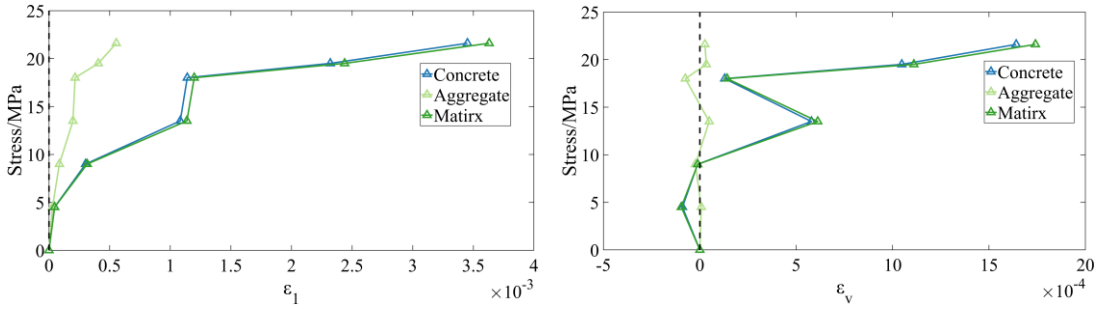

(a) (b)

Fig. 17. Strain vs. macroscopic stress histories. (a) Average maximum principal strain vs. macroscopic stress of each phase. (b) Average volumetric strain vs. macroscopic stress of each phase.

5.2 Local Region of Interest

Considering computational efficiency, 340 slices with a radius of 8.9 mm from 15.6 mm to 30.9 mm along the *z*-axis were kept for the analysis of damage, and the corresponding volume was 4.75 cm^3. The DVC resolution was improved by reducing the mesh size (Hild, et al., 2012). The mean element size was equal to 11 vx, and ℓ_{reg} was equal to 90 vx, with 51,680 elements and 56,315 nodes. The heterogeneous weighting *C* for heterogeneous Reg-C8-DVC is reported in Table 3. For the kinematic analyses, the sections indicated in Fig. 3(d,f) (white dashed box) are used for illustration purposes.

5.2.1 Damage Analysis Based on Strain Fields

The damaged elements are shown in Fig. 18. They are based on the processing route discussed in Section 5.1.3. The maximum principal strain field analysis based on the reduced region of interest is used to analyze the influence of loading on the internal deformation of concrete and damage growth.

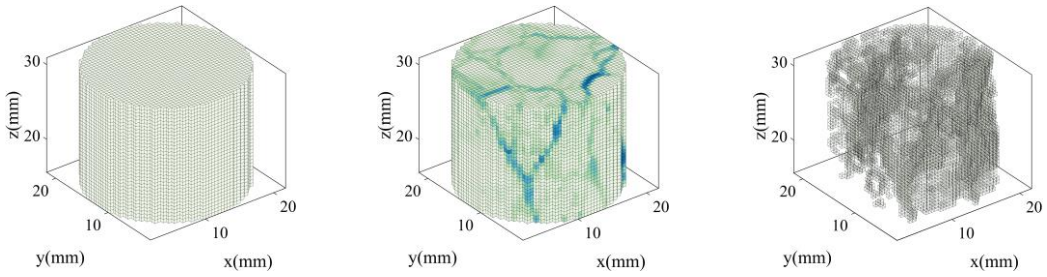

(a) (b) (c)

Fig. 18 Identification of damaged elements. (a) Reference GLR field. (b) Comparison GLR field. (c) Damaged elements.

Fig. 20 displays the changes in maximum principal strain in concrete (Fig. 19) for applied

stresses equal to 9.0, 13.5, 18.0, 19.5, and 21.6 MPa. At 9.0 MPa (i.e., 40% of the ultimate strength, Fig. 20(a)), the strain concentration zone indicated by the yellow dashed regions appears clearly. Compared to Fig. 19(b, d), it is observed that the main strain concentration region was on the interface between the aggregates and matrix and around pores at this stage. When the applied stress increased to 13.5 MPa (i.e., 60% of the ultimate strength, Fig. 20(b)), the strain concentration region developed and new regions (blue dashed boxes) appeared. When the stress continued to increase to 18.0 MPa (i.e., 80% of the ultimate strength, Fig. 20(c)), some cracked regions temporarily closed. It is observed that the strain concentrations in some areas (white dashed box) exhibited a decreasing trend. Then, with the continuous increase of stress to 19.5 MPa (i.e., 87% of the ultimate strength, Fig. 20(d)), the strain concentrations in the existing damaged regions further increased and continued to expand. When the stress increased to 21.6 MPa (i.e., 96% of the ultimate strength, Fig. 20(e)), the internal non-uniform deformation of the concrete further aggravated, and the sample approached failure. From the *YZ* section, regions A and B are interphases between aggregates and matrix, which are the weakest phases of concrete, the strain concentration was high when the applied load increased. Region C is a pore region, which corresponds to initial damage of concrete. There were strain concentrations on the edge of the pore. Combined with Fig. 19(b,d), the strain concentration area corresponds to the failure morphology of some concrete sections.

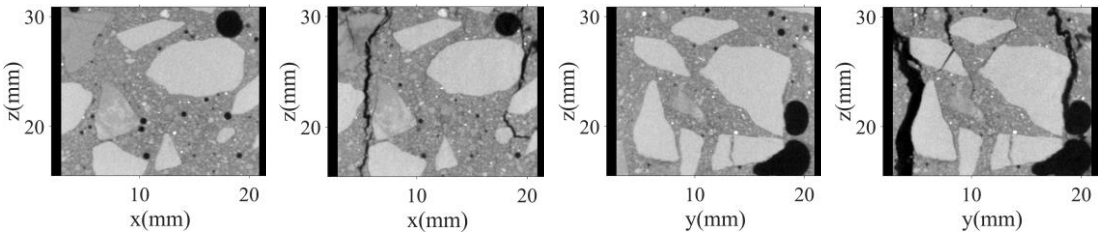

(a) (b) (c) (d)

Fig. 19 ROI sections located at y = 12.5 mm at 0 MPa (a) and after failure (b) and the ROI section located at x = 12.5 mm at 0 MPa (c) and after failure (d).

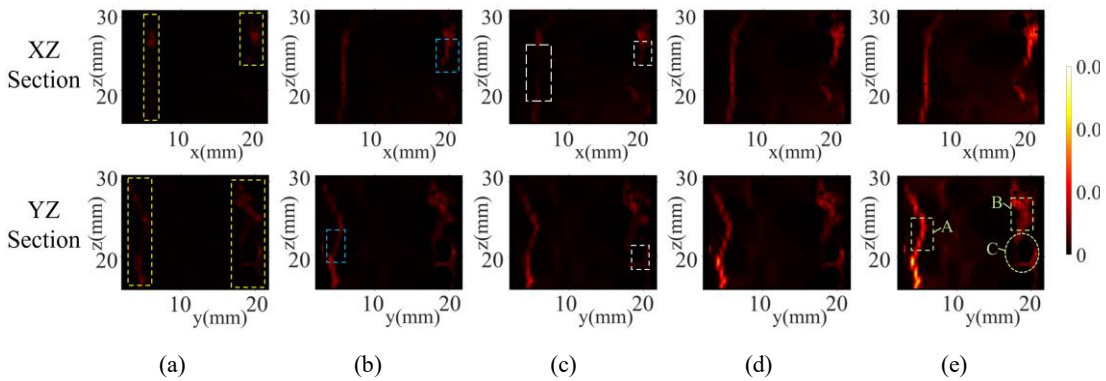

Fig. 20. Sections of maximum principal strains during damage development.

(a) 9.0 MPa, (b) 13.5 MPa, (c) 18.0 MPa, (d) 19.5 MPa, (e) 21.6 MPa.

5.2.2 Damage Analysis

The newly generated microcrack network was obtained using Equation (16) and is plotted in Fig. 21. The COD detection uncertainty is defined as 5 times the standard COD uncertainty (only for damaged elements) for heterogeneous Reg-C8-DVC considering damage, which was equal to 0.26 vx. The regions with COD levels less than the detection uncertainty were made transparent. Further, COD fields correspond to a direct measure of newly generated microcracks, their propagation, and coalescence. Therefore, the formation of Fracture Process Zone (FPZ) is characterized via subvoxel resolved CODs. As a consequence, the damage network evolving in space, time and material phases can be constructed.

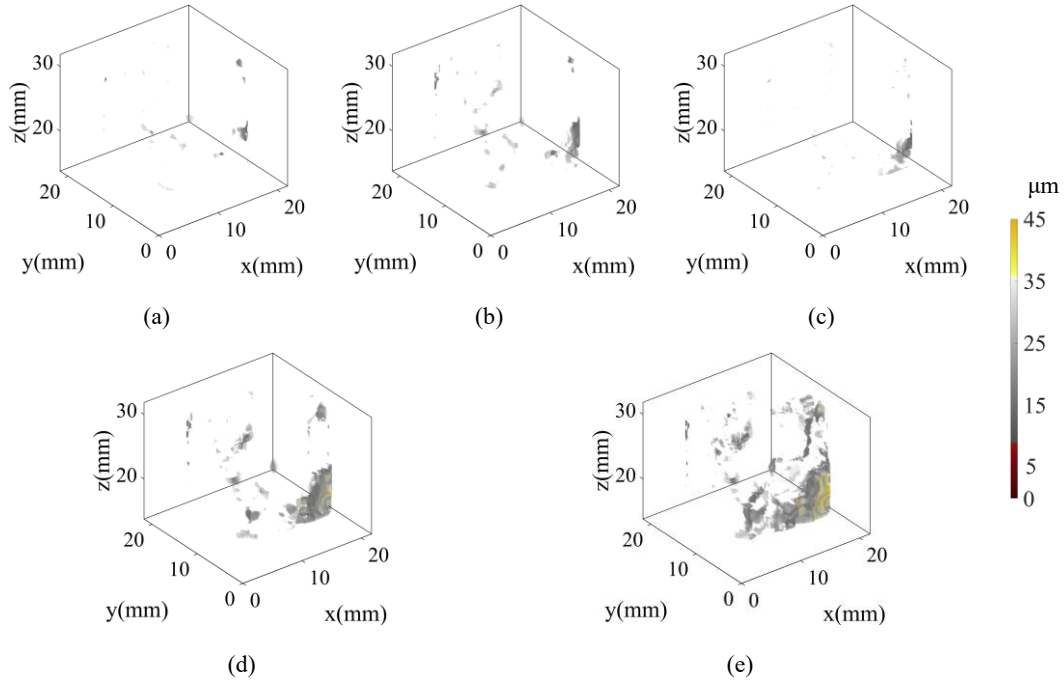

Fig. 21. Newly generated microcrack network during damage growth.

(a) 9.0 MPa, (b) 13.5 MPa, (c) 18.0 MPa, (d) 19.5 MPa, (e) 21.6 MPa.

The volume changes in subvoxel- and voxel-level crack openings at each loading stage are reported in Table 4. When subvoxel-level openings are involved, only the voxels in which they are located were used for the statistical analyses.

Table 4 Statistics of volume changes of microcracks.

Stress (MPa)	Total crack		Subvoxel-level crack		Voxel-level crack	
	volume (mm^3)	proportion (‰)	volume (mm^3)	proportion (‰)	volume (mm^3)	proportion (‰)
9.0	3.4	0.7	3.4	0.7	0	0
13.5	11.4	2.4	11.4	2.4	0	0
18.0	5.3	1.1	5.3	1.1	0	0
19.5	43.7	9.2	43.6	9.2	0.1	0.02
21.6	85.4	18.0	82.7	17.4	2.7	0.6

The microcrack volumes and percentages in the aggregates, matrix, and interfacial transition zones (ITZs) are statistically analyzed and listed in Table 5. ITZs are further studied as the main failure area (Königsberger, et al., 2018) and are typically 20 to 100 μm thick (Zhou, et al., 2023). However, considering that the DVC mesh size is 11 vx, the ITZs in this work correspond to elements sharing aggregate/matrix interfaces. The maximum FPZ length was statistically measured using the length of the smallest cuboid containing the FPZ. The FPZ lengths for each loading stage, along with the average and standard deviations of the COD within each FPZ were statistically analyzed and their histograms are displayed in Table 6.

Table 5 Statistics of microcrack volume fractions in each phase.

Stress (MPa)	Total volume (mm^3)	Maximum FPZ length (mm)	Matrix		ITZ		Aggregate	
			volume (mm^3)	proportion (%)	volume (mm^3)	proportion (%)	volume (mm^3)	proportion (%)
9.0	3.4	2.8	0.2	7.1	3.0	87.8	0.2	5.0
13.5	11.4	6.7	1.0	8.7	10.3	90.4	0.1	1.0
18.0	5.3	5.3	0.9	17.8	4.3	81.5	0.04	0.8
19.5	43.7	11.3	8.1	18.5	35.3	80.9	0.3	0.6
21.6	85.4	17.6	26.4	30.9	58.7	68.7	0.3	0.4

Table 4 and Table 5 show that when the applied stress was equal to 9.0 MPa and 13.5 MPa, the

microcracks grew slowly, corresponding to the initiation and early development steps. At this stage, only subvoxel openings occurred, accounting for 0.7‰ and 2.4‰ of the volume of the region of interest, respectively. The cracks essentially developed in the ITZs, and accounted for 87.8% and 90.4% of the total cracked volume. The maximum FPZ lengths were 2.8 mm and 6.7 mm, respectively. This result shows that ITZs have poor mechanical properties. When the applied stress increased to 18.0 MPa, the total cracked volume and maximum FPZ length decreased to reach 6.2 mm^3 and 1.4 mm, indicating a local compressive region. Thus, some microcracks temporarily closed. When the applied stress reached 19.5 MPa, the microcracks propagated rapidly, the total cracked volume and maximum FPZ length increased by 38.4 mm^3 and 6 mm, indicating that the cracks had entered the stage of unstable propagation. The proportion of microcracks in the ITZs slightly decreased from 81.5% to 80.9%, whereas that in the matrix increased from 17.8% to 18.5%. Moreover, voxel-level openings appeared at this time in a volume of 0.1 mm^3. When the applied stress was equal to 21.6 MPa, the opening amplitude of microcracks further augmented, the total cracked volume and maximum FPZ length grew to 41.7 mm^3 and 6.3 mm. The total volume fraction of microcracks accounted for 18‰, the proportion of subvoxel openings was 17.4‰ (i.e., 97% of total cracked volume), and the voxel-level opening volume was 2.7 mm^3. The microcrack activity in the matrix was significant, with the proportion rising rapidly to 30.9%, thereby indicating that the matrix had become the main region for damage growth. The ITZs were still the most severely damaged area, and the microcrack volume in that area accounted for 68.7% (twice that of the matrix). Throughout the loading process, the aggregates experienced the lowest damage activity. Last, at the macroscopic elastic stage (i.e., 4.5 MPa or 20% of the ultimate strength), subvoxel openings were detected and the microcracked volume was very small (1.39 mm^3). It is worth noting that this study focused on measuring the internal damage of concrete before the peak load based on DVC analyses. Due to the quasi-brittle nature of concrete, capturing internal damage beyond the peak is very challenging via in situ tests. Additionally, the post-mortem configurations typically result in very large CODs, making DVC calculations difficult to converge. Based on crack segmentation, the cracked volume fraction after the peak load was found to be equal to 1.2×10^3 mm^3.

As the stress gradually increased from 9.0 MPa to 21.6 MPa, the evolution of internal damage in concrete exhibited complexity and non-uniformity, which specifically manifested itself in the changes of distributions of FPZ length and COD (Table 6). When the applied stress was equal to 9.0

MPa, the FPZ length primarily concentrated within the range of 0-1.3 mm, with a small number of cracks around 2.5 mm already emerging. The average and standard CODs were of the order of 0.013 mm and 10^{-3} mm, respectively, indicating that the crack openings were relatively small and uniform at this stage. When the stress increased to 13.5 MPa, the main peak of the FPZ length distribution reached 21 instances and the maximum FPZ length extended to 6.7 mm, suggesting continuous crack propagation. The average and standard CODs exhibited even more pronounced long-tail characteristics, with maximum values of 1.7×10^{-2} mm and 3.8×10^{-3} mm, respectively, reflecting the non-uniform expansion process of the crack network. For the applied stress equal to 18.0 MPa, the FPZ length distribution became more concentrated, the main peak height and maximum length slightly decreased. The average COD was primarily distributed within the range $[1.2, 1.4] \times 10^{-2}$ mm. Meanwhile, the distribution displayed more pronounced multi-peak features. This phenomenon may be related to the temporary closure of some microcracks due to local compression, and also reflects the increasing complexity and non-uniformity of the crack network. When the applied stress reached 19.5 MPa, the main peak height of the FPZ length distribution decreased to 15 instances. The mean and standard CODs were significantly higher than those in the early loading stages, and the maximum length rose to 11.3 mm, indicating rapid expansion of the crack network. The maximum values of average and standard CODs were equal to 2.0×10^{-2} mm and 7.1×10^{-3} mm, respectively, suggesting that not only did the CODs increase, but their scatter also further widened in different regions. Last, for an applied stress of 21.6 MPa, the main peak range of FPZ length was [0.28, 0.42] mm, with a mean, standard deviation and maximum of FPZ length surging to 1.1, 2.0 and 17.6 mm, respectively, thereby demonstrating the formation of a large-scale continuous crack network. The maximum values of the average and standard CODs were 2.2×10^{-2} mm and 1.0×10^{-2} mm, respectively, reflecting the highly complex characteristics of the crack network, which encompassed a wide distribution ranging from small microcracks to large-scale penetrating cracks.

Table 6 Distribution of FPZ length and COD characteristics at each loading stage.

Stress (MPa)	FPZ length	Average COD	Standard COD
9.0	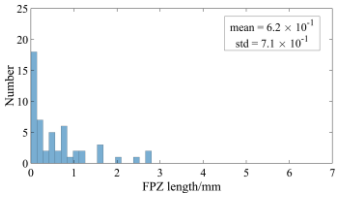	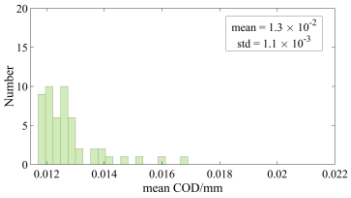	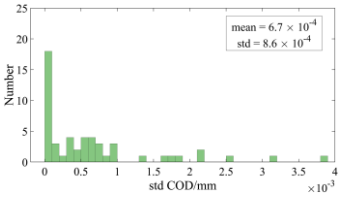
13.5	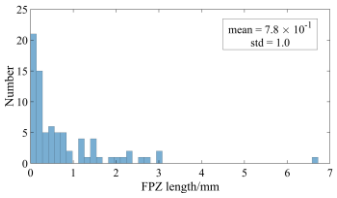	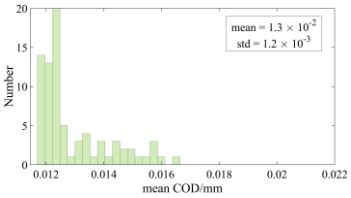	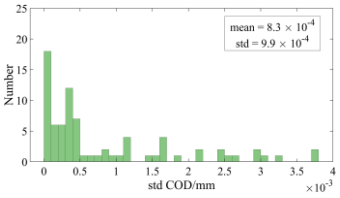
18.0	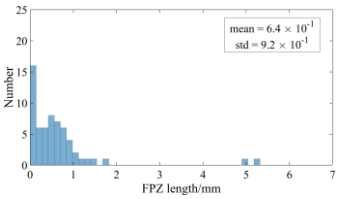	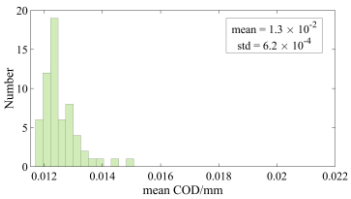	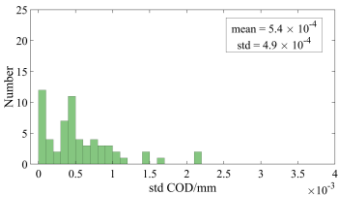
19.5	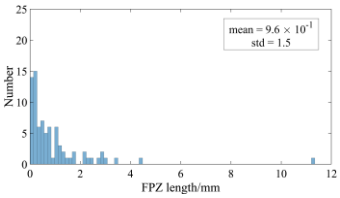	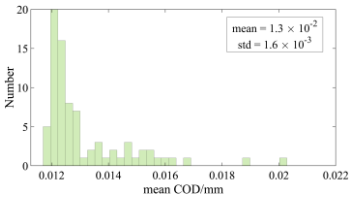	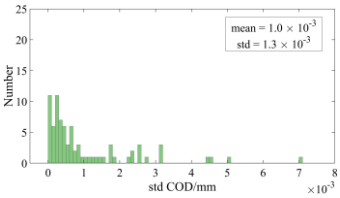
21.6	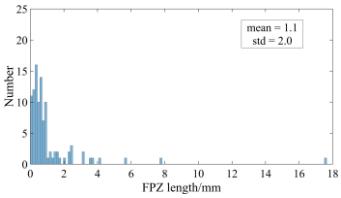	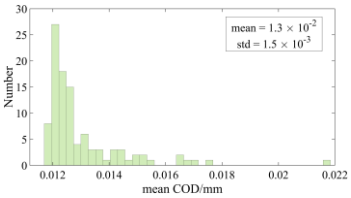	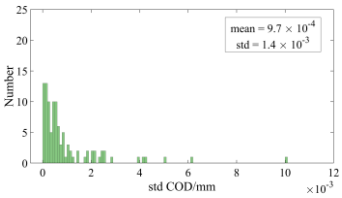

The afore-mentioned results show that the FPZ in the concrete quantified via DVC is different from the FPZs in specimens with pre-existing cracks in three-point flexural tests, chevron cracked notched Brazilian tests, and uniaxial compression tests (Zhang, et al., 2022). Instead, multiple tiny, scattered microcracks are observed. The distribution of cracks with very small openings indicates that the damaged zone is not made of a single propagating crack, but results from a complex and hierarchical process. This process is related to the load steps and all concrete phases, with an early focus on developmental expansion in ITZs, gradually extending into the matrix. The characterization method based on subvoxel COD resolution provides a basis for constructing crack

networks associated with FPZs under 3D complex stress states.

5.2.3 Damage and Failure

As the weakest region inside concrete, the ITZs tend to spontaneously initiate damage before the other regions, which significantly affect the mechanical properties and cracking behavior of concrete. As a porous material, the concrete pore characteristics also have non negligible influences on its mechanical properties. Therefore, this study analyzes the deformation characteristics of the ITZ and edge of the pore.

Fig. 22 displays the average maximum principal strain in the ITZs and the region around pores (elements within a 11 vx range of the pore edge) at each loading stage. During initial loading, the strain concentrations on the edges of the pores is higher those that in the ITZs. With increased stress, new cracks initiate and propagate in the ITZs. At later loading stages, the strain concentrations in the ITZs become higher. The average maximum principal strain in the ITZs is 6.7×10^{-3}, whereas that close to the pores is 5.3×10^{-3} for a macroscopic stress of 21.6 MPa.

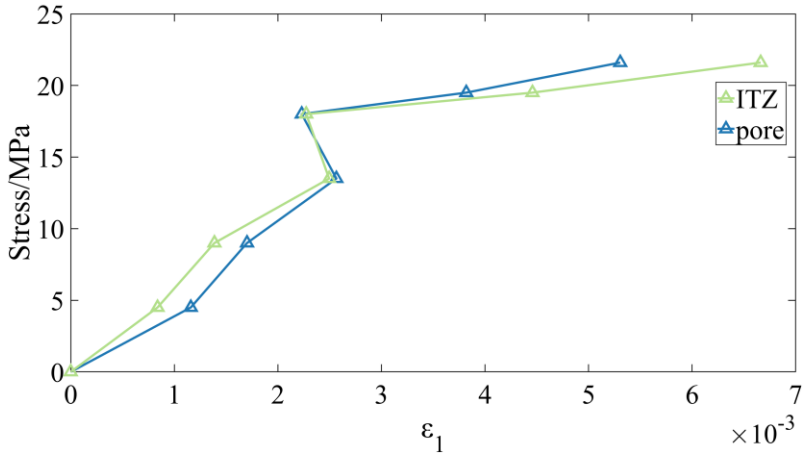

Fig. 22. Average maximum principal strain vs. macroscopic stress in the ITZs and around pores.

Typical local CT image slices of the interior of concrete before and after damage and the corresponding strain field slices (21.6 MPa) were selected for a detailed analysis. In Table 7(a, b), owing to the difference in mechanical responses between the aggregates and the matrix, high displacement gradients occur on the interfaces. The strain concentrations in the ITZs are significantly higher than those in the surrounding regions. The ITZs generally exhibit poor mechanical properties. By combining the data in the CT image after failure, it is found that a through

crack with large CODs is formed in ITZs. As illustrated in Table 7(b), under the influence of different ITZs, the crack bifurcates and changes directions many times.

Table 7 Concrete gray-level image and strain field sections.

Serial number	CT Slice before loading	Strain field at 21.6 MPa	CT Slice after failure
a	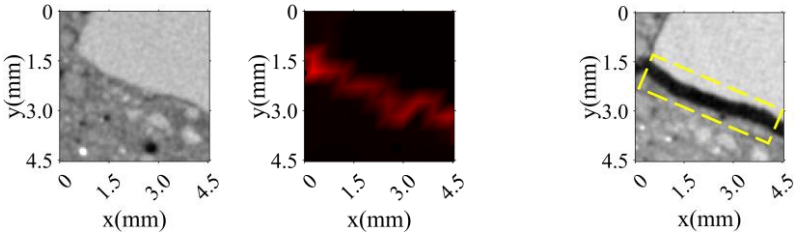		
b	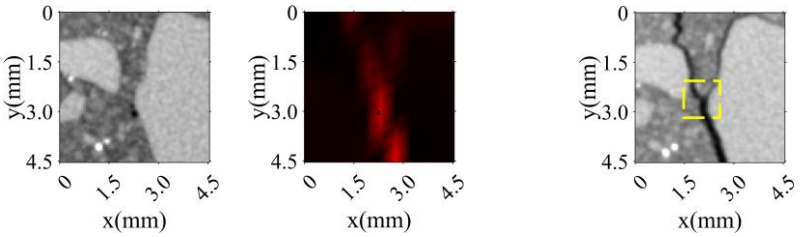		
c	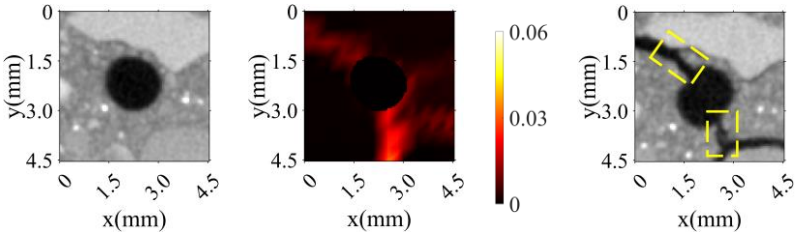		
d	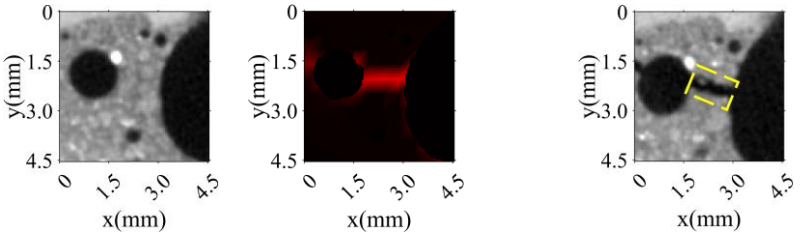		
e	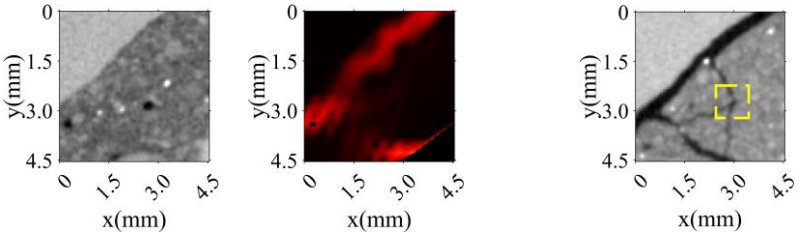		

In Table 7(c), because the pore is located between an aggregate and the matrix, the pore and ITZ form a weak region, resulting in non-uniform deformation and high strain concentrations.

Furthermore, the pore plays a bridging role to connect two cracks in the ITZs. When the sample fails, the CODs in this region is often large. Table 7(d) shows that the coexistence of two large pores produces a weak zone. The interaction between the pores creates a high strain concentration region, eventually leading to a crack.

In Table 7(e), the strain concentration in the yellow dashed box is relatively small because the pore is completely located in the matrix. In the CT slice after failure, although no large penetrating crack passes through the pore, small cracks from the pore region connect with large ones in the ITZ. This effect is due to the fact that the damaged zone always expands to the weakest surrounding regions. When the damage zone develops near pores, it affects their surroundings, which are already in a high strain state, and initiate secondary cracks.

The fracture process of concrete consists in the expansion of cracks dominated by one or more damaged zones, during which secondary cracks are continuously initiated. The above analysis shows that the damage zone that caused concrete failure was mainly formed in the ITZ, whereas the pore region played a synergistic driving role.

6 Conclusion

In this study, mechanically regularized DVC considering elastic heterogeneity and damage was utilized to study an in-situ experiment to measure 3D deformation fields inside a concrete sample under uniaxial compression. The visualization and quantification of the formation of new microcracks in the material bulk during the entire loading process was obtained and studied.

The following conclusions were drawn:

(1) Considering elastic heterogeneity and damage improved the faithfulness of mechanically regularized Reg-C8-DVC. The highest standard displacement uncertainty was 3×10^{-3} vx, and the highest standard strain uncertainty was 2×10^{-5} for the selected regularization length. Subvoxel-level openings (above 0.26 vx) were quantified for newly generated microcracks.

(2) Non-uniform characteristics of the internal deformation of concrete were revealed through strain fields. The average maximum principal and volumetric strains in the matrix were higher than those in the aggregates. There were strain concentrations in the ITZ and around pores. With an increase in applied stress, the strain concentrations in the ITZs were significantly higher than those around pores. The degradation of the ITZs dominated the development of damage, whereas the pores

played a synergistic driving role in damage and failure.

(3) At 20% and 87% of the ultimate strength, cracks initiated with subvoxel- and voxel-level openings, respectively. At 96% of the ultimate strength, the volume fraction of microcracks was 18‰, of which 97% were containing subvoxel-level microcrack openings. The proportions of microcracks in the matrix, ITZs, and aggregates were 30.9, 68.7, and 0.4%, respectively.

(4) With consideration of elastic heterogeneity and damage, Reg-C8-DVC enables for detailed analyses and quantifications of deformation fields and damage of FPZs in concrete. The distribution of cracks with very small openings was revealed and indicated that the damaged zone is not a single propagating crack, but a complex and hierarchical process.

Funding

This work was financially supported by the National Key Research and Development Program of China (2022YFC2904102), Science Fund for Creative Research Groups of the National Natural Science Foundation of China (52121003), and Key Laboratory of Coal Gangue Resource Utilization and Energy - Saving Building Materials of Liaoning (LNTUCEM-2302).

Conflicts of interest

The authors declare no conflict of interest.

Author Contributions

Shangyu Yang: Conceptualization, Methodology, Investigation, and Writing-Original Draft. **Haizhou Liu:** Methodology and Investigation; **Lingtao Mao:** Resources, Conceptualization, Validation, Supervision and Writing-Review; **Fangao Li**: Formal analysis and Investigation; **Bingjie Wei**: Formal analysis and Investigation; **Yang Ju:** Resources and Supervision; **François Hild:** Validation, Supervision and Writing-Review.

References

Brandt, A.M. Cement-Based Composites: Materials, Mechanical Properties and Performance[M]. CRC pres s, 2005.

Burud, N.B., J.C. Kishen, Response Based Damage Assessment Using Acoustic Emission Energy for Plain Concrete, Constr Build Mater 269 (2021) 121241.

Chateau, C., T.T. Nguyen, M. Bornert, J. Yvonnet, Dvc-Based Image Subtraction to Detect Microcracking in Lightweight Concrete, Strain 54 (2018) e12276-.

Chung, S.-Y., J.-S. Kim, P.H. Kamm, D. Stephan, T.-S. Han, M. Abd Elrahman, Pore and Solid Character izations of Interfacial Transition Zone of Mortar Using Microcomputed Tomography Images, J Mater Civ Eng 33 (12) (2021).

Claisse, P.A. Civil Engineering Materials[M]. Butterworth-Heinemann, 2015.

Ding, W., L. Zhu, H. Li, M. Lei, F. Yang, J. Qin, A. Li, Relationship between Concrete Hole Shape and Meso-Crack Evolution Based on Stereology Theory and Ct Scan under Compression, Materials (Basel) 15 (16) (2022).

du Plessis, A., W.P. Boshoff, A Review of X-Ray Computed Tomography of Concrete and Asphalt Construction Materials, Constr Build Mater 199 (2019) 637-651.

Gercek, H., Poisson's Ratio Values for Rocks, Int J Rock Mech Min Sci 44 (1) (2007) 1-13.

Germaneau, A., P. Doumalin, J.-C. Dupré, 3d Strain Field Measurement by Correlation of Volume Images Using Scattered Light: Recording of Images and Choice of Marks, Strain 43 (3) (2007) 207-218.

Giaccio, G., R. Zerbino, Failure Mechanism of Concrete: Combined Effects of Coarse Aggregates and Strength Level, Adv Cem Based Mater 7 (2) (1998) 41-48.

Golewski, G.L., Evaluation of Fracture Processes under Shear with the Use of Dic Technique in Fly Ash Concrete and Accurate Measurement of Crack Path Lengths with the Use of a New Crack Tip Tracking Method, Measurement 181 (2021) 109632.

Gupta, M., M. Sharma, B. Shashank, Multiscale Modelling of Uniaxial Compressive Stress-Strain Behaviour of Concrete Using Analytical Homogenisation and Damage Mechanics, Mech Mater 173 (2022) 104430.

He, B., H.G. Zhang, X.P. Zhu, Q.M. Zheng, O. Onuaguluchi, N. Banthia, Z.W. Jiang, Thermal-Dependent Brittleness Effect of Ultra-High Performance Concrete Exposed to Cryogenic Flexural Loads by Acoustic Emission Evaluation, Cem Concr Compos 139 (2023) 105056.

Hild, F., A. Bouterf, S. Roux, Damage Measurements Via Dic, Int J Fract 191 (2015) 77-105.

Hild, F., S. Roux, Comparison of Local and Global Approaches to Digital Image Correlation, Exp Mech 52 (9) (2012) 1503-1519.

Hild, F., S. Roux. Digital Image Correlation[M]. 2012.

Hong, S., P. Liu, J. Zhang, F. Xing, B. Dong, Visual & Quantitative Identification of Cracking in Mortar Subjected to Loads Using X-Ray Computed Tomography Method, Cem Concr Compos 100 (2019) 15-24.

Hong, S., J. Weng, S. Peng, J. Zhang, B. Dong, Visualized Evaluation of Mechanical Bonding Properties of Cementitious Material Interfaces Based on Volumetric Strain Analysis, Cem Concr Compos 130 (2022).

Hong, S.X., C. Kuang, J.C. Zhang, B.Q. Dong, Segmentation Method for Enhancing the Continuity and Integrality of Microcracks in Concrete Fracture Xct Image, J Mater Civ Eng 34 (3) (2022) 04021478.

Ji, S., L. Li, H.B. Motra, F. Wuttke, S. Sun, K. Michibayashi, M.H. Salisbury, Poisson's Ratio and Auxetic Properties of Natural Rocks, Journal of Geophysical Research: Solid Earth 123 (2) (2018) 1161-1185.

Jiroušek, O., I. Jandejsek, D. Vavřík, Evaluation of Strain Field in Microstructures Using Micro-Ct and Digital Volume Correlation, J Instrum 6 (01) (2011) C01039.

Jivkov, A.P., D.L. Engelberg, R. Stein, M. Petkovski, Pore Space and Brittle Damage Evolution in Concrete, Eng Fract Mech 110 (2013) 378-395.

Königsberger, M., M. Hlobil, B. Delsaute, S. Staquet, C. Hellmich, B. Pichler, Hydrate Failure in Itz Governs Concrete Strength: A Micro-to-Macro Validated Engineering Mechanics Model, Cem Concr Res 103 (2018) 77-94.

Leclerc, H., J.-N. Périé, F. Hild, S. Roux, Digital Volume Correlation: What Are the Limits to the Spatial Resolution?, Mech Ind 13 (6) (2012) 361-371.

Leclerc, H., J.-N. Périé, S. Roux, F. Hild, Voxel-Scale Digital Volume Correlation, Exp Mech 51 (2011) 479-490.

Li, P.-D., Y.-F. Wu, Damage Evolution and Full-Field 3d Strain Distribution in Passively Confined Concrete, Cem Concr Compos 138 (2023).

Lian, H., X. Sun, Z. Yu, Y. Lian, L. Xie, A. Long, Z. Guan, Study on the Dynamic Fracture Properties and Size Effect of Concrete Based on Dic Technology, Eng Fract Mech 274 (2022) 108789.

Liu, H., L. Mao, Y. Ju, F. Hild, Damage Evolution in Coal under Different Loading Modes Using Advanced Digital Volume Correlation Based on X-Ray Computed Tomography, Energy (2023) 127447.

Lorenzoni, R., V.N. Lima, T.C.S. Figueiredo, M. Hering, S. Paciornik, M. Curbach, V. Mechtcherine, F. de Andrade Silva, Macro and Meso Analysis of Cement-Based Materials Subjected to Triaxial and Uniaxial Loading Using X-Ray Microtomography and Digital Volume Correlation, Constr Build Mater 323 (2022) 126558.

Mao, L., H. Liu, Y. Lei, J. Wu, Y. Ju, F.-P. Chiang, Evaluation of Global and Local Digital Volume Correlation for Measuring 3d Deformation in Rocks, Rock Mech Rock Eng 54 (9) (2021) 4949-4964.

Mao, L., Z. Yuan, M. Yang, H. Liu, F.-p. Chiang, 3d Strain Evolution in Concrete Using in Situ X-Ray Computed Tomography Testing and Digital Volumetric Speckle Photography, Measurement 133 (2019) 456-467.

Mao, L.T., F.-p. Chiang, Mapping Interior Deformation of a Composite Sandwich Beam Using Digital Volumetric Speckle Photography with X-Ray Computed Tomography, Compos Struct 179 (2017) 172-180.

Mazars, J., A Description of Micro-and Macroscale Damage of Concrete Structures, Eng Fract Mech 25 (5-6) (1986) 729-737.

Minguet, C., F. Soulas, T. Lafargue-Tallet, E. Chalumeau, M. Pommies, R. Peiffer, F. Hild, On the Validation of a Priori Estimates of Standard Displacement Uncertainties in T3-Stereocorrelation, Meas Sci Technol 32 (2) (2020) 024004.

Oesch, T., F. Weise, G. Bruno, Detection and Quantification of Cracking in Concrete Aggregate through Virtual Data Fusion of X-Ray Computed Tomography Images, Materials 13 (18) (2020) 3921.

Ouyang, X., Z. Wu, B. Shan, Q. Chen, C. Shi, A Critical Review on Compressive Behavior and Empirical Constitutive Models of Concrete, Constr Build Mater 323 (2022) 126572.

Qin, L., C. Guo, W. Sun, X. Chu, T. Ji, H. Guan, Identification of Damage Mechanisms of Polymer-Concrete in Direct Shearing Tests by Acoustic Emission, Constr Build Mater 351 (2022) 128813.

Ronneberger, O., P. Fischer, T. Brox. U-Net: Convolutional Networks for Biomedical Image Segmentation [C]//Medical Image Computing and Computer-Assisted Intervention–MICCAI 2015: 18th International Conference, Munich, Germany, October 5-9, 2015, Proceedings, Part III 18. Springer. 2015: 234-241.

Stamati, O., E. Roubin, E. Andò, Y. Malecot, P. Charrier, Fracturing Process of Micro-Concrete under Uniaxial and Triaxial Compression: Insights from in-Situ X-Ray Mechanical Tests, Cem Concr Res 149 (2021) 106578.

Sun, Q., B. Martin, B. Williams, W. Heard, D. Frew, X. Nie, Comparative Study on the Impact-Induced Microstructural Damage in Concrete Using X-Ray Computed Micro-Tomography, Mech Mater 168 (2022) 104277.

Tian, W., N. Han, Analysis on Meso-Damage Processes in Concrete by X-Ray Computed Tomographic Scanning Techniques Based on Divisional Zones, Measurement 140 (2019) 382-387.

Tsitova, A., F. Bernachy-Barbe, B. Bary, S. Dandachli, C. Bourcier, B. Smaniotto, F. Hild, Damage Quant

ification Via Digital Volume Correlation with Heterogeneous Mechanical Regularization: Application to an in Situ Meso-Flexural Test on Mortar, Exp Mech (2022) 1-17.
van Dijk, N.P., D. Wu, C. Persson, P. Isaksson, A Global Digital Volume Correlation Algorithm Based on Higher-Order Finite Elements: Implementation and Evaluation, Int J Solids Struct 168 (2019) 211-227.
Wong, R.C.K., K.T. Chau, Estimation of Air Void and Aggregate Spatial Distributions in Concrete under Uniaxial Compression Using Computer Tomography Scanning, Cem Concr Res 35 (8) (2005) 1566-1576.
Zhang, F., Y. Yang, S.A. Fennis, M.A. Hendriks, Developing a New Acoustic Emission Source Classification Criterion for Concrete Structures Based on Signal Parameters, Constr Build Mater 318 (2022) 126163.
Zhang, J.-Z., X.-P. Zhou, Fracture Process Zone (Fpz) in Quasi-Brittle Materials: Review and New Insights from Flawed Granite Subjected to Uniaxial Stress, Eng Fract Mech 274 (2022) 108795.
Zhang, J., C. Kuang, Z. Liu, C. Lin, K. Wang, S. Hong, B. Dong, D. Hou, L. Liu, F. Xing, Evolutionary Trace for Ductile Fracture Performance of Rubber− Cement Composites, Cem Concr Compos 121 (2021) 104080.
Zhang, Y., X. Chen, J. Zhou, Q. Wang, Z. Liu, Z. Ma, J. Huang, Meso-Scale Damage Characteristics of Low Carbon Concrete with Recycled Aggregate Based on in-Situ Ct Test, Constr Build Mater 365 (2023) 130014.
Zhou, G., Z. Xu, 3d Mesoscale Investigation on the Compressive Fracture of Concrete with Different Aggregate Shapes and Interface Transition Zones, Constr Build Mater 393 (2023) 132111.
Zhou, K., D. Lei, J. He, P. Zhang, P. Bai, F. Zhu, Real-Time Localization of Micro-Damage in Concrete Beams Using Dic Technology and Wavelet Packet Analysis, Cem Concr Compos 123 (2021) 104198.
Zienkiewicz, O.C., R.L. Taylor, J.Z. Zhu. The Finite Element Method: Its Basis and Fundamentals[M]. Elsevier, 2005.